

Spin-Polarized Resonant Tunneling in Antiferromagnetic Heterojunctions of Graphene Nanoribbons with 3d Adatoms

Francisco Sánchez-Ochoa^{ID*}

Departamento de Materia Condensada, Instituto de Física, Universidad Nacional Autónoma de México, Apartado Postal 20-364, Cd. de México C.P. 01000, Mexico



(Received 6 May 2022; revised 25 August 2022; accepted 27 October 2022; published 21 November 2022)

Binding, magnetic, and electron transport properties of 3d transition-metal (TM) adatoms (Cr-Cu) on an antiferromagnetic armchair graphene nanoribbon heterojunction are studied by means of density-functional-theory (DFT) calculations and nonequilibrium Green function (NEGF) formalism. The heterojunction emulates a system of two symmetric potential barriers and one well with resonances (quasibound states). Binding energies show a strong interaction between 3d TM adatoms and heterojunction hollow sites, where 3d TM adatoms prefer the edges rather than the middle of the graphene heterojunction. As for magnetic properties, heterojunctions with Cr, Mn, and Fe have a ferromagnetic behavior with a total magnetic moment $\geq 4\mu_B$, while Co, Ni, and Cu adatoms induce antiferromagnetism in the full system with total magnetizations $< 3\mu_B$. Transmission curves show that electronic resonances undergo a spin-splitting effect induced by 3d TM adatoms, and current versus bias-voltage curves show spin currents from which spin-polarized ratios (SPRs) $> 75\%$ for Co and approximately 100% for Ni adatoms are calculated. Finally, an oscillatory behavior is observed in SPR curves at low bias due to a combined effect of resonant tunneling and spin filtering. Therefore, these results suggest that the present antiferromagnetic graphene heterojunction with Co and Ni adatoms is suitable for future spin and low-power nanoelectronics as a spin-dependent resonant tunneling device.

DOI: [10.1103/PhysRevApplied.18.054068](https://doi.org/10.1103/PhysRevApplied.18.054068)

I. INTRODUCTION

With the rise of graphene at the beginning of the 21st century [1], other one-dimensional (1D) atomic structures derived from graphene, such as nanoribbons, have emerged as promising candidates for spintronic nanodevices owing to weak spin-orbit coupling and hyperfine interaction of carbon atoms as well as high carrier mobility and band-gap tuning [2–4]. Finite 1D carbon heterojunctions can be built fusing segments of graphene nanoribbons with different widths, lengths, and edge terminations (armchair, zigzag, or chiral edges) [5–7]. In particular, a consecutive append process of armchair graphene nanoribbon (AGNR) segments with different widths and fixed length create a 1D graphene heterojunction. This is because AGNRs are semiconductors with tuneable electronic band gaps. The band-gap size in AGNRs is a function of the ribbon width [8–10]. AGNRs can be grouped into three different subfamilies, that is, $N = 3p$, $N = 3p + 1$, and $N = 3p + 2$, where p is an integer and N the number of carbon atom pairs across the AGNR [10]. While the $N = 3p$ and $N = 3p + 1$ families have wide band gaps that scale inversely with the ribbon width, the family $N = 3p + 2$ is

predicted with narrow band gaps by *ab initio* calculations or with a metallic behavior if the tight-binding method is used [10].

Interesting phenomena have been studied in AGNR heterojunctions, such as negative differential conductivity [11–14] due to resonant tunneling, resonance splitting [12,15,16], Wannier-Stark ladders [14], optical excitations [17], and topological states [5,18,19]. Covalent edge-bonded AGNRs of different band-gap sizes generate a potential profile with barriers and wells for charge carriers. Hence, electrons and holes experience a potential profile with the same periodicity as the heterojunction. The smallest symmetric heterojunction consists of two potential barriers and one well [20–22], where quasibound states (electronic resonances) are generated inside the well [12]. The number of bound states and the energy separation between them depend on the geometrical parameters of the system. In this context, the study and design of more complex 1D nanostructures with AGNRs, such as lateral heterojunctions, is an interesting issue to address in order to develop interconnection components with vanishing band gaps and modern high-speed electronic devices as diodes or transistors [7]. Computational and experimental efforts, mainly bottom-up assembly of AGNRs from molecular precursors, have been

*fsanchez@fisica.unam.mx

done to explore quantum effects [6,9,13,23–25] and their potentiality [17,26,27].

In this work, a 1D lateral heterojunction with two potential barriers and one quantum well is built, using the width of AGNRs as a key factor for band-gap engineering, and then adsorb on it 3d transition metal (TM) atoms (magnetic impurities). This is in order to study spin ground-state properties using total energy density-functional-theory (DFT) calculations. After that, the nonequilibrium Green function (NEGF) formalism is used to calculate conductance and spin-resolved current versus bias-voltage curves. Conductance results show that electronic resonances undergo spin (exchange) splitting, which can be tuned due to strong 3d TM atom adsorption on edges of graphene heterojunctions. The spin-splitting effect leads to spin-polarized currents, and this, in turn, leads to SPR values > 50% for Co and Ni adatoms. Moreover, oscillations are observed in SPR curves at low bias and can be interpreted as a spin-dependent resonant tunneling effect.

II. METHODOLOGY

First the structural relaxation of periodic graphene heterojunction using collinear spin-polarized DFT as implemented in the SIESTA code [28,29] is studied. The electronic states are expanded using a linear combination of numerical atomic orbitals (LCAOs) with a single- ζ plus polarized (SZP) basis set. Exchange and correlation energies are treated with the Perdew-Burke-Ernzerhof (PBE) [30] functional within the generalized gradient approximation (GGA). Norm-conserving Trouiller-Martins [31] pseudopotentials are used to describe core-valence electron interactions. A $1 \times 1 \times 7 k$ grid is used for sampling the reciprocal space with the Monkhorst-Pack scheme [32], and an energy cutoff of 300 Ry for the grid integration of charge density in real space. The electronic temperature is set equal to 100 K with a Fermi-Dirac statistics. The atomic relaxation is achieved when the interatomic forces are ≤ 20 meV/Å, while the electronic relaxation is converged to 10^{-4} . A vacuum gap of 15 Å in the lateral (x and y) directions is used to prevent interactions between neighbor AGNR heterojunctions in adjacent supercells. Visualization of atomic models and isosurfaces is performed with the VESTA program [33].

Once the ground-state properties of pristine heterojunctions and 3d TM atom-doped heterojunctions are calculated with DFT, then the electron transport properties are determined with the NEGF formalism implemented in the Transiesta module [34]. The calculation of the Hamiltonian for left and right electrodes is done using an $1 \times 1 \times 1001 k$ grid. Employing the previous self-consistent Hamiltonian, the current, I_σ , calculation is performed at finite bias voltage, V_b , by means of the Landauer-Buttiker

formula [35],

$$I_\sigma(V_b) = G_0 \int_{\mu_L}^{\mu_R} T_\sigma(E, V_b) [f(E, \mu_L) - f(E, \mu_R)] dE, \quad (1)$$

where σ represents the spin degree of freedom, $G_0 = e^2/h$ is the conductance quantum, e is the electric charge, and h is Planck's constant. $T_\sigma(E, V_b)$ is the transmission coefficient at energy E and bias $V_b = (\mu_L - \mu_R)/e$, f is the Fermi distribution function, and $\mu_{L,R}$ are the chemical potentials of the left and right electrodes, with $\mu_L = E_F + V_b/2$ and $\mu_R = E_F - V_b/2$. E_F is set to zero. The $T_\sigma(E, V_b)$ coefficient is calculated as follows:

$$T_\sigma(E, V_b) = \text{Tr} [\Gamma_L(E, V_b) G(E, V_b) \Gamma_R(E, V_b) G^\dagger(E, V_b)], \quad (2)$$

with $G(E, V_b)$ [$G^\dagger(E, V_b)$] the retarded (advanced) Green's function and $\Gamma_{L,R}$ are coupling matrices. To compute the $I_\sigma(V_b)$ curves we use the previous converged density matrix (with lower V_b) to start an alternative calculation of I_σ (with higher V_b) to achieve a better self-consistent convergence. Furthermore, the imaginary part of the device states, η , is set to 0.01 eV to achieve electron self-consistency for nonequilibrium calculations as well. Finally, $T_\sigma(E, V_b)$, or equivalently the conductance $G = G_0 T_\sigma(E, V_b)$, and $I_\sigma(V_b)$ through the device are calculated using the postprocessing tool TBTrans [34].

III. RESULTS

The periodic graphene heterojunction is sketched in Fig. 1(a), where the left and right electrodes, enclosed by orange rectangles, and the scattering region at the middle can be identified. For the construction of the electrodes and potential well, the first member of the $N = 3p + 2$ family with $p = 1$ is taken into account. Both potential well and electrodes are made of narrow band-gap semiconductors with five pairs of carbon atoms, hereafter five AGNR, meanwhile the potential barriers are built up taking the third element of the $N = 3p$ family with $p = 3$, or nine AGNR. The nine-AGNR structure should be a wider band-gap semiconductor [10,12], see Fig. 1(a). The central region contains six units of five AGNR while the potential barriers have only two units of nine AGNR with carbon edges saturated by hydrogen atoms. The schematic representation of the potential profile is shown above the atomic model in Fig. 1(a) with some energy levels (E_0, E_1 , and E_2) denoting quasibound states [12]. After the atomic relaxation of pristine and nonmagnetic graphene heterojunction, the ferromagnetic state and two antiferromagnetic configurations are studied, because zigzag edges are present at the interface between nine-AGNR and five-AGNR segments. Figures 1(b) and 1(c) show the local spin density, $\sigma(\mathbf{r}) = \rho(\mathbf{r})_\uparrow - \rho(\mathbf{r})_\downarrow$ with $\rho(\mathbf{r})_\uparrow(\rho(\mathbf{r})_\downarrow)$ being the

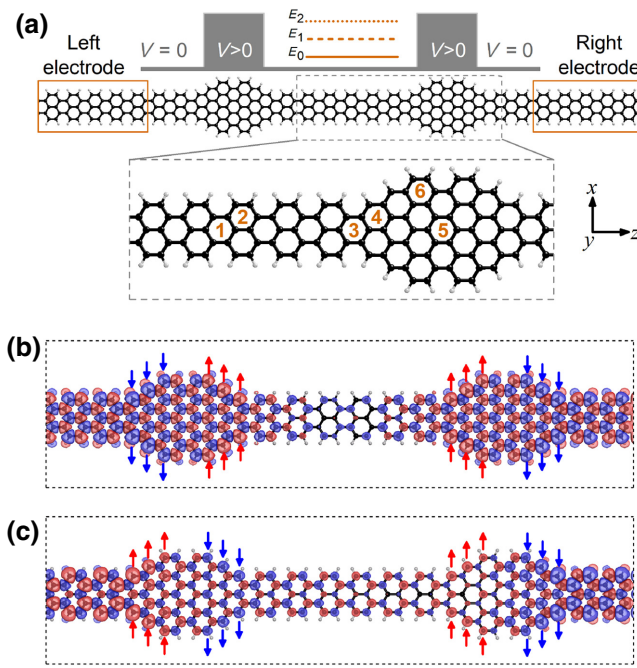


FIG. 1. (a) Atomic model of graphene heterojunction with left and right electrodes sandwiching the scattering region. Two nine-AGNR segments sandwiching the central region with six five-AGNR units. The dashed gray rectangle shows a magnification of the atomic model with six hollow sites labeled in orange where $3d$ TM atoms can be adsorbed. Carbon and hydrogen atoms are colored by black and white, respectively. Panels (b) and (c) show two antiferromagnetic configurations where the local spin density, $\sigma(\mathbf{r})$, is plotted with red (blue) color for majority (minority) spin, using an isosurface value of $\pm 2.5 \times 10^{-6}$ and $\pm 7 \times 10^{-7} \text{ e}/\text{Å}$ for (b) and (c), respectively. Red and blue arrows depict the spin orientation of $\sigma(\mathbf{r})$ on carbon atoms at zigzag edges.

majority (minority) charge density, of two antiferromagnetic configurations. The antiferromagnetic configuration in Fig. 1(c) is the ground state. This magnetic configuration shows an antiferromagnetic exchange coupling along the heterojunction and a ferromagnetic coupling between zigzag edges across the heterojunction, in agreement with a previous report [36]. Notice that, the magnetic configuration in Fig. 1(c) shows a first-neighbor antiferromagnetic exchange coupling. However, the spin configuration in Fig. 1(b) shows a small frustration at the center of the potential well with ferromagnetic coupling between nearest-neighbor carbon atoms.

The hollow site is the energetically most stable site found in previous theoretical reports [37,38] to adsorb some of the present $3d$ TM atoms (Co, Cr, Fe, and Mn), instead top and bridge sites, in graphene monolayer as well as in AGNRs. On the other hand, we can compare the calculated adsorption energy trends for the graphene heterojunction + $3d$ TM adatoms with sites 1 and 2 (sites 5 and 6) with those results of adsorption energy trends

for periodic five AGNRs and nine AGNRs reported in Ref. [37]. The additional calculations of binding energy for sites 3 and 4 are performed to address the interface between five AGNRs and nine AGNRs. Thus, from Refs. [37,38], we expect the $3d$ TM atoms tend to be preferentially adsorbed on edges and in hollow sites instead the center or at intermediate hollow sites of the graphene heterojunction. Therefore, for symmetry and simplicity, only the six hollow sites labeled in Fig. 1(a) are studied to deposit $3d$ TM atoms: Cr-Cu. To measure the interaction strength between the $3d$ TM atoms and the graphene heterojunction, the binding energy calculation is performed using [39]

$$E = E_{\text{HJ+atom}} - E_{\text{HJ}} - E_{\text{atom}} + \delta_{\text{BSSE}}, \quad (3)$$

where $E_{\text{HJ+atom}}$ is the total energy of the heterojunction+TM adatom system, E_{HJ} is the energy of the pristine heterojunction and E_{atom} is the energy of the isolated TM atom. The last term in Eq. (3), δ_{BSSE} , is an energy correction needed to remove artificial interactions between TM adatoms and the heterojunction since we are using a finite basis set of atomic orbitals. To calculate δ_{BSSE} , we follow the procedure as in Refs. [39,40] taking into account the basis-set superposition error (BSSE) of Boys and Bernardi [41].

Figure 2(a) shows the calculated binding energies for various $3d$ TM atoms on different hollow sites of the graphene heterojunction. As can be seen from Fig. 2(a), a strong interaction is observed due to binding energies $>0.75 \text{ eV}$ for Fe, Co and Ni atoms, meanwhile Cr, Mn, and Cu atoms show binding energies of approximately 1.5 eV. In general, from Fig. 2(b), the most stable hollow site is 2 from Mn to Cu. Cr atom can adsorb on several hollow sites, from site 1 to 4. Notice that, $3d$ TM atoms tend to be adsorbed on edges of five AGNRs and at the interface between five AGNRs and nine AGNRs. The binding energy trend and the most stable configuration found here are in good agreement with results reported in Ref. [37], as well as in graphene monolayer [42] and zigzag GNRs [43]. Strong binding energies can be ascribed to C($2p$)-TM atom hybridization through $3d$ orbitals. It is noteworthy to mention that Fe, Ni, and Co adatoms prefer the edges instead of the middle of the heterojunction as in zigzag graphene nanoribbons [43–45], but more noticeable is that Mn and Fe adatoms show a similar relative energy trend, see Fig. 2(b), as well as the pair Co and Ni adatoms. Hence, we observe that Mn, Fe, Co, and Ni atoms are adsorbed on edges. In addition, a relative energy of >50 (<50) meV between site 2 and site 4 for Co and Ni (Mn and Fe) atoms is observed. This means that site 2 is the most energetically stable site to adsorb Co and Ni atoms, while Fe atoms can adsorb on site 1, 3, or 4, due to the small relative energy among these sites.

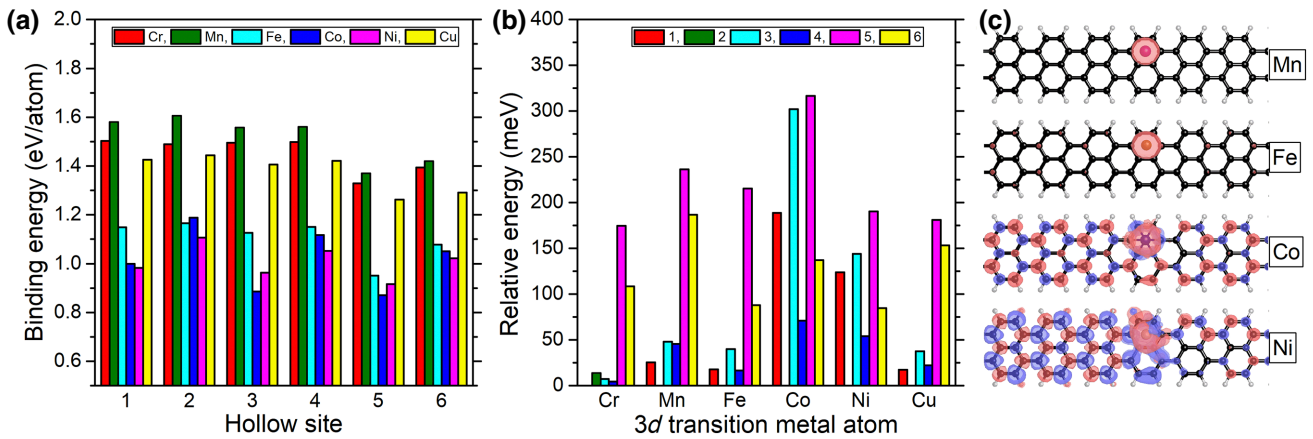


FIG. 2. (a) Absolute value of binding energy and (b) relative energy of 3d TM atoms on different hollow sites labeled by numbers. The system with the highest binding energy is taken as the reference, 0 eV, in the relative energy plot. (c) Ground-state $\sigma(\mathbf{r})$ around 3d TM atoms adsorbed on site 2. The isosurface values are 0.07, 0.05, 0.005, and 0.001 for Mn, Fe, Co, and Ni, respectively. The majority (minority) spin component is plotted with red (blue) color.

Table I shows the outer-shell electronic configuration and magnetic moment (in bold) of isolated 3d TM atoms, the total magnetization of the full system and the magnetic moment of adsorbed 3d TM atom. Additionally, Table I shows a proposal of electronic configuration and magnetic moment for 3d TM atoms after the adsorption process with integer occupancies. Firstly, as already known from $\text{Cr}(3d^54s^1)$ to $\text{Cu}(3d^{10}4s^1)$ the number of electrons increases in the 3d shell but the total magnetic moment decreases by the Pauli exclusion principle and Hund's rule, see the first column in Table I. Second, after the adsorption of 3d TM atoms on different hollow sites, the full system remains with a magnetization greater than $4\mu_B$ for Cr, Mn, and Fe, meanwhile the graphene heterojunction with Co, Ni, or Cu adatoms has a total magnetization less than $3\mu_B$. In particular, the graphene heterojunction with Co, Ni, and Cu adatoms on different sites achieves > 1 , 0, and $1\mu_B$, respectively; in good agreement with other reports on 3d TM atom-doped zigzag GNRs [43,45]. Although Mn and Fe atoms increase their magnetic moment, see Fig. 2(c); Cr, Co, Ni, and Cu atoms tend to decrease their magnetization when deposited on the graphene heterojunction, but they induce a $\sigma(\mathbf{r})$ on neighbor carbon atoms with

opposite spin, such as Co and Ni, see Fig. 2(c). Interestingly, graphene heterojunctions with Ni adatoms have a null magnetization showing an antiferromagnetic spin configuration between Ni adatoms and neighbor carbon rings, see Fig. 2(c). Conversely, Cu-doped graphene heterojunction shows a ferromagnetic behavior similar to Mn and Fe atoms in Fig. 2(c).

A Mulliken population analysis is performed to understand the nature of the interaction between TM adatoms and graphene heterojunction. The resulting Mulliken charges for Cr, Mn, Fe, Co, Ni, and Cu adatoms are in average 5.06, 6.22, 7.21, 7.69, 8.77, and 10.06e, respectively, which means electron withdrawing from 3d TM atoms towards the heterojunction of approximately 1e at first insight, in agreement with other reports on graphene [42]. From the previous analysis, a proposal of electronic configuration and magnetic moment for TM adatoms is shown in the eighth column of Table I, where a $4s \rightarrow 3d$ charge-transfer mechanism of 1e is observed for Co and Ni adatoms in addition to 1e transferred to the heterojunction. The Cu adatom has a half-filled 3d shell after 1e charge transfer from 4s orbital towards the graphene heterojunction. Mn adatoms have

TABLE I. First column: outer-shell electronic configuration and magnetic moment (in μ_B) of isolated 3d TM atoms. From second to seventh column: total magnetic moment for full system (first value in bold) and atom contribution (second value) for several hollow sites. Eighth column: proposal of electronic configuration and magnetic moment for adsorbed TM atoms on graphene heterojunction.

Isolated TM atom	Site 1	Site 2	Site 3	Site 4	Site 5	Site 6	Adsorbed TM atom
$\text{Cr}(3d^54s^1) - 6$	4.01 , 4.87	5.86 , 4.89	4.04 , 4.86	4.15 , 4.87	5.86 , 4.88	4.20 , 4.87	$\text{Cr}(3d^54s^0) - 5$
$\text{Mn}(3d^54s^2) - 5$	5.01 , 5.89	6.98 , 5.92	6.86 , 5.89	5.15 , 5.90	6.88 , 5.92	5.15 , 5.91	$\text{Mn}(3d^54s^1) - 6$
$\text{Fe}(3d^64s^2) - 4$	4.00 , 4.86	5.99 , 4.89	5.78 , 4.80	4.14 , 4.88	4.46 , 4.89	4.06 , 4.87	$\text{Fe}(3d^64s^1) - 5$
$\text{Co}(3d^74s^2) - 3$	1.00 , 2.15	2.99 , 2.23	2.96 , 2.35	2.71 , 2.21	1.45 , 2.16	1.10 , 2.13	$\text{Co}(3d^84s^0) - 2$
$\text{Ni}(3d^84s^2) - 2$	0.00 , 0.58	0.00 , 0.41	0.00 , 0.61	0.00 , 0.52	0.00 , 0.23	0.00 , 0.36	$\text{Ni}(3d^94s^0) - 1$
$\text{Cu}(3d^{10}4s^1) - 1$	0.98 , 0.00	0.98 , 0.00	0.90 , 0.00	0.83 , 0.01	0.84 , 0.00	0.74 , 0.01	$\text{Cu}(3d^{10}4s^0) - 0$

the highest magnetic moment, $6\mu_B$, because its $4s$ orbital losses $1e$.

Once the ground-state properties are discussed, the electron transport properties of the $3d$ TM atom-doped graphene heterojunction are determined. The average conductance of pristine graphene heterojunction, with the antiferromagnetic configuration of Fig. 1(c), is shown in Fig. 3. We observe one and two symmetric electronic resonances at 0 eV and near ± 0.2 eV, respectively. From now on, we focus on two $3d$ TM atom-doped systems with the highest binding energy from Fig. 2(a) [or systems with relative energy close to zero in Fig. 2(b)]; in other words, those with $3d$ TM atoms adsorbed on sites 2 and 4, despite the Cr system. Figures 3(a) and 3(b) depict the spin-resolved conductance for graphene heterojunctions with $3d$ TM atoms on sites 2 and 4, respectively. Notice that, strong changes are observed in conductance above and below the Fermi energy in comparison with that of pristine heterojunction, but a well-defined and non-degenerate peak is observed just at the Fermi level. Far from the Fermi level, the nonoverlapping of electronic resonances between majority and minority spin components shown in Fig. 3 is due to a Zeeman-like effect induced by magnetic adatoms on graphene heterojunctions. This is a strong spin-splitting effect for electronic resonances above and below the Fermi level. The conductance peaks just at the Fermi level are considered as zero-mode resonances in the literature [12,18] and here leads to charge delocalization in five-AGNR electrodes. The absence of the spin-splitting effect for the zero-energy resonance can be

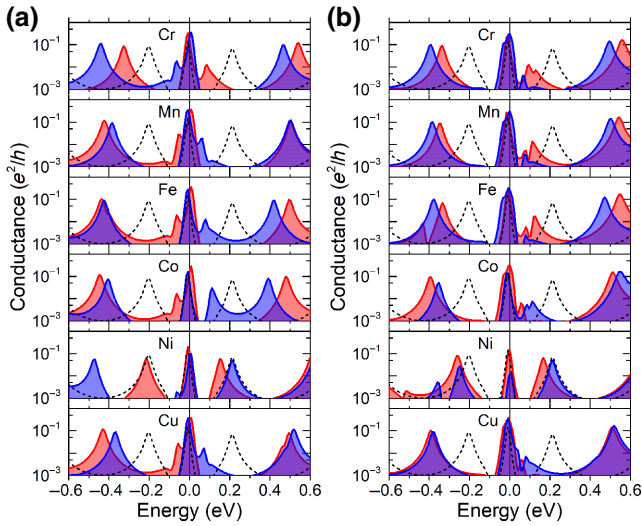


FIG. 3. Spin-resolved conductance components versus energy of $3d$ TM adatoms on (a) site 2 and (b) site 4 of graphene heterojunction. Majority and minority spin components are plotted in red and blue, respectively. Conductance of pristine heterojunction is plotted with dashed black lines for comparison. The Fermi energy is at 0 eV.

ascribed to electrodes without near TM adatoms, however small differences in conductance amplitudes for majority and minority spins are observed at the Fermi level for Co and Ni. In particular, when Ni atom is adsorbed on site 4, see Fig. 3(b), the conductance amplitude of majority spin is $\simeq 10$ greater than the minority component. In addition, a tiny spin splitting at the Fermi level is observed when TM atoms are adsorbed on site 2, but the spin-splitting effect is stronger for those first resonances near the Fermi energy. It is noteworthy to mention that the presence of $3d$ states gives antiresonances in the valence regime for the majority spin component at -0.4 eV (minority spin at -0.3 eV) when Fe (Ni) atom is adsorbed on site 4 of graphene heterojunction.

The quantum resonant tunneling effect for pristine graphene heterojunction is observed in Fig. 4, where the maximum of the electron current is at approximately 0.4 V [12]. This bias value is approximately twice the energy value of the first resonances in Fig. 3 divided by electron charge. Spin-resolved current versus bias-voltage curves are plotted in Fig. 4 for sites 2 (blue) and 4 (green). From 0 to 0.1 V, both spin-current components (majority and minority) decrease as the bias increases with a current enhancement for all cases, in comparison with the current of pristine graphene heterojunction, except for the Ni case. The current enhancement effect is due to electron

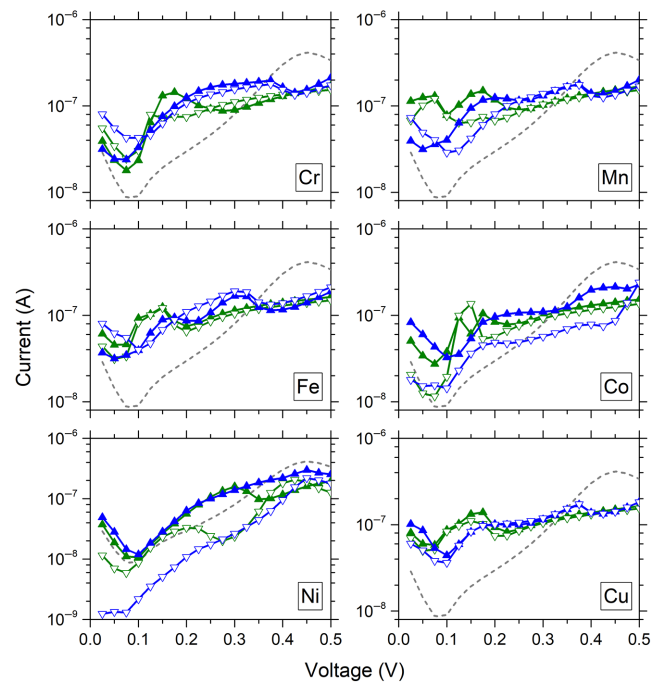


FIG. 4. Spin-resolved current components versus bias voltage for TM adatoms on site 2 (4) in green (blue) with filled (empty) triangles denoting majority (minority) spin. The average current of pristine graphene heterojunction is plotted with dashed lines for comparison.

charge transfer from $3d$ TM atoms towards the graphene heterojunction as discussed above. However, even when Ni adatoms do not show current enhancement at low bias, the Ni adatom strongly attenuates the minority spin-current component when adsorbed on site 4. For $V_b > 0.1$ V, the current for Cr, Fe, and Cu atoms on heterojunction tends to be the same for both majority and minority spin components until $V_b \simeq 0.5$ V. As can be seen in Fig. 4, the current curves of majority and minority spin components for Mn, Co, and in particular Ni almost do not overlap at low voltages, which means that a spin-filtering effect can be achieved. The Ni adsorption process on site 4 is the most interesting case since current curves of both spins do not overlap. To highlight the difference between majority (I_{up}) and minority spin currents (I_{dn}), the spin-polarization ratio (SPR) [46] is calculated, also known as spin-filtering efficiency (SFE) [47], which is the capacity of a device to pass a particular spin-current component:

$$P(V_b) = 100\% \times \left| \frac{I_{\text{up}}(V_b) - I_{\text{dn}}(V_b)}{I_{\text{up}}(V_b) + I_{\text{dn}}(V_b)} \right|. \quad (4)$$

Figure 5 shows the SPR for low bias without the SPR value at 0 eV to avoid the discontinuity in Eq. (4). Notice that, all TM adatoms on sites 2 and 4 enable a spin-filtering effect with a $\text{SPR} \geq 25\%$, being the Cu adatom with the lowest SPR value and Ni adatom with the highest SPR value (almost 100% for voltages less than 0.1 V). Ni and Co adatoms allow the current flow of the majority spin component with a small current contribution of minority spin component until 0.15 V whenever Ni and Co adatoms are on site 4, nevertheless the SPR achieves values $\leq 50\%$ for Ni and Co adatoms on site 2 for bias < 0.15 V. When Cr, Mn, and Fe atoms are adsorbed on site 4, the SPR shows an oscillatory behavior reaching values between approximately 25% and $\simeq 50\%$. To show the robustness of the SPR effect in heterojunctions with $3d$ TM adatoms, we further calculate the SPR for site 1 since Mn, Fe, and Cu atoms have a small relative energy difference between sites 1 and 2, see Fig. 2(b). As shown in Fig. 5, while Cr, Mn, and Cu adatoms show a decreasing spin-filtering effect till 0.15 V, Ni shows an almost perfect (approximately 100%) spin-filtering effect in a wide voltage range having a small current dip at 0.325 V. Hence, the SPR for Fe, Co, and Ni atoms on site 1 is greater than on sites 2 and 4 for low bias. The high SPR values for Ni are due to backscattering processes for the minority spin component induced by the localized $3d$ states. Owing to the charge transfer from $3d$ TM atoms to graphene heterojunction, the electronic resonances undergo an energy down shift and the spin degeneracy is lifted. This, in turn, leads to a spin-polarized resonant tunneling effect since SPR oscillations are observed [48,49]. Therefore, owing to their open $3d$ -shell configuration of TM atoms, the adsorption mechanism of $3d$ TM atoms can be considered a viable route

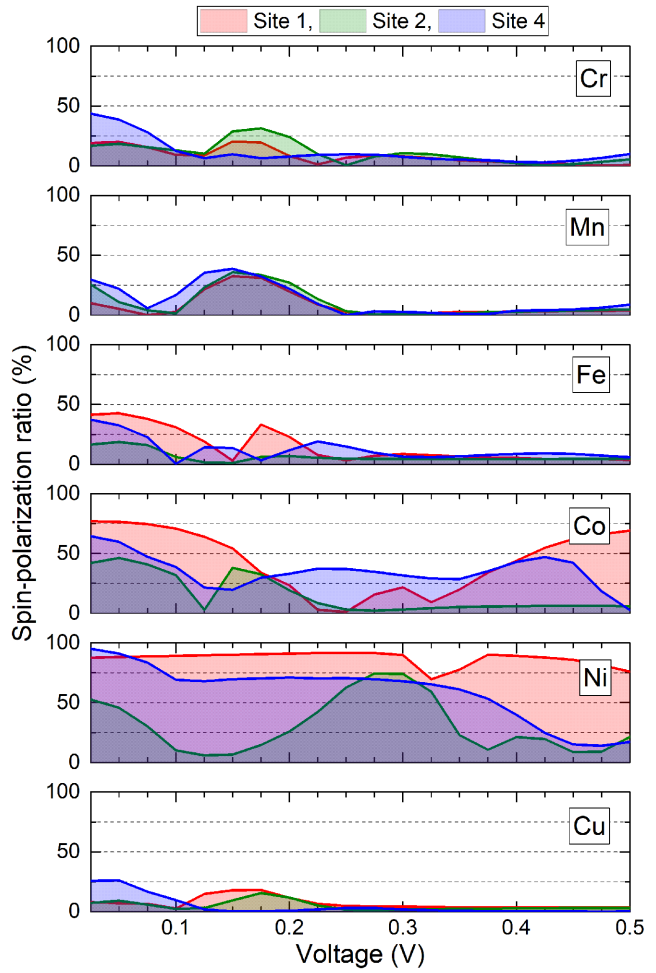


FIG. 5. Spin-polarization ratio for all TM atoms adsorbed on site 1 (red), site 2 (green), and site 4 (blue).

to obtain spin-polarized currents in these graphene heterojunctions instead of a precise and hard control of edges in experiments [50,51]. Let us mention that this magnetic graphene heterojunction with Co or Ni adatoms can be considered as a candidate material to study spin-flip [52] or spin-relaxation effects [53], topological states [5,18,19], and spininterfaces [54] from which organic semiconductors are adsorbed on ferromagnetic substrates.

IV. CONCLUSIONS

In summary, we calculate the binding, magnetic, and transport properties of AGNR heterojunctions using density functional theory and the nonequilibrium Green function formalism, in order to show that the present 1D graphene systems doped with $3d$ TM atoms behave as spin-polarized resonant tunneling diodes. Using the width of AGNRs as a key factor, we show that electronic resonances are present in these devices through the conductance in the scattering region, which can be tuned by spin and energy via adsorption of $3d$ TM atoms. We observe an

increment in conductivity of 3d TM-doped graphene heterojunction due to electron charge transfer from 3d TM atoms. Indeed, this effect enhances spin-polarized currents with SPR approximately 100% at low voltages for Ni, due to a backscattering effect of minority spin component by localized 3d states, and an oscillatory behavior of SPR from Cr to Fe. Therefore, devices made of AGNRs doped with 3d TM atoms can be considered as promising interconnects in chips with low electric power consumption in modern nano (spin) electronics of high performance. Finally, we expect the present results motivate experimentalists to synthesize this antiferromagnetic graphene heterojunction for future studies and applications.

ACKNOWLEDGMENTS

We thank Michael Springborg and Raul Esquivel for fruitful discussions. The authors acknowledge the computer resources, technical expertise, and support provided by the Laboratorio Nacional de Supercómputo del Sureste de México, CONACYT member of the network of national laboratories.

-
- [1] A. K. Geim and K. S. Novoselov, The rise of graphene, *Nat. Mater.* **6**, 183 (2007).
 - [2] C. L. Kane and E. J. Mele, Quantum Spin Hall Effect in Graphene, *Phys. Rev. Lett.* **95**, 226801 (2005).
 - [3] D. Huertas-Hernando, F. Guinea, and A. Brataas, Spin-orbit coupling in curved graphene, fullerenes, nanotubes, and nanotube caps, *Phys. Rev. B* **74**, 155426 (2006).
 - [4] J. Fischer, B. Trauzettel, and D. Loss, Hyperfine interaction and electron-spin decoherence in graphene and carbon nanotube quantum dots, *Phys. Rev. B* **80**, 155401 (2009).
 - [5] D. J. Rizzo, G. Veber, T. Cao, C. Bronner, T. Chen, F. Zhao, H. Rodriguez, S. G. Louie, M. F. Crommie, and F. R. Fischer, Topological band engineering of graphene nanoribbons, *Nature* **560**, 204 (2018).
 - [6] Y.-C. Chen, T. Cao, C. Chen, Z. Pedramrazi, D. Haberer, D. G. De Oteyza, F. R. Fischer, S. G. Louie, and M. F. Crommie, Molecular bandgap engineering of bottom-up synthesized graphene nanoribbon heterojunctions, *Nat. Nanotechnol.* **10**, 156 (2015).
 - [7] P. H. Jacobse, A. Kimouche, T. Gebraad, M. Ervasti, J. Thijssen, P. Liljeroth, and I. Swart, Electronic components embedded in a single graphene nanoribbon, *Nat. Commun.* **8**, 1 (2017).
 - [8] K. Nakada, M. Fujita, G. Dresselhaus, and M. S. Dresselhaus, Edge state in graphene ribbons: Nanometer size effect and edge shape dependence, *Phys. Rev. B* **54**, 17954 (1996).
 - [9] P. Kim, M. Y. Han, A. F. Young, I. Meric, and K. L. Shepard, in *2009 IEEE International Electron Devices Meeting (IEDM)* (IEEE, 2009), p. 1.
 - [10] Y.-W. Son, M. L. Cohen, and S. G. Louie, Energy Gaps in Graphene Nanoribbons, *Phys. Rev. Lett.* **97**, 216803 (2006).
 - [11] F. Sánchez-Ochoa, G. H. Cocoletzi, and G. Canto, in *Chemical Modelling* (The Royal Society of Chemistry, 2021), Vol. 16, p. 100.
 - [12] F. Sanchez-Ochoa, J. Zhang, Y. Du, Z. Huang, G. Canto, M. Springborg, and G. H. Cocoletzi, Ultrananow heterojunctions of armchair-graphene nanoribbons as resonant-tunnelling devices, *Phys. Chem. Chem. Phys.* **21**, 24867 (2019).
 - [13] S. Li, C. K. Gan, Y.-W. Son, Y. P. Feng, and S. Y. Quek, Low-bias negative differential resistance effect in armchair graphene nanoribbon junctions, *Appl. Phys. Lett.* **106**, 013302 (2015).
 - [14] G. J. Ferreira, M. N. Leuenberger, D. Loss, and J. C. Egues, Low-bias negative differential resistance in graphene nanoribbon superlattices, *Phys. Rev. B* **84**, 125453 (2011).
 - [15] C. H. Pham and V. L. Nguyen, Tunneling through finite graphene superlattices: Resonance splitting effect, *J. Phys.: Condens. Matter* **27**, 095302 (2015).
 - [16] Y. Xu, Y. He, and Y. Yang, Resonant peak splitting in graphene superlattices with one-dimensional periodic potentials, *Appl. Phys. A: Mater. Sci. Process.* **115**, 721 (2014).
 - [17] D. Prezzi, D. Varsano, A. Ruini, and E. Molinari, Quantum dot states and optical excitations of edge-modulated graphene nanoribbons, *Phys. Rev. B* **84**, 041401 (2011).
 - [18] J.-P. Joost, A.-P. Jauho, and M. Bonitz, Correlated topological states in graphene nanoribbon heterostructures, *Nano Lett.* **19**, 9045 (2019).
 - [19] T. Cao, F. Zhao, and S. G. Louie, Topological Phases in Graphene Nanoribbons: Junction States, Spin Centers, and Quantum Spin Chains, *Phys. Rev. Lett.* **119**, 076401 (2017).
 - [20] R. Tsu and L. Esaki, Tunneling in a finite superlattice, *Appl. Phys. Lett.* **22**, 562 (1973).
 - [21] L. Chang, L. Esaki, and R. Tsu, Resonant tunneling in semiconductor double barriers, *Appl. Phys. Lett.* **24**, 593 (1974).
 - [22] J. González, L. Rosales, and M. Pacheco, Resonant states in heterostructures of graphene nanoribbons, *Phys. B: Condens. Matter* **404**, 2773 (2009).
 - [23] A. F. Young and P. Kim, Quantum interference and Klein tunnelling in graphene heterojunctions, *Nat. Phys.* **5**, 222 (2009).
 - [24] H. Sevinçli, M. Topsakal, and S. Ciraci, Superlattice structures of graphene-based armchair nanoribbons, *Phys. Rev. B* **78**, 245402 (2008).
 - [25] G. Saha, A. K. Saha, and A. B. M. H.-U. Rashid, in *2015 IEEE 15th International Conference on Nanotechnology (IEEE-NANO)* (IEEE, 2015), p. 440.
 - [26] A. Kimouche, M. M. Ervasti, R. Drost, S. Halonen, A. Harju, P. M. Joensuu, J. Sainio, and P. Liljeroth, Ultrananow metallic armchair graphene nanoribbons, *Nat. Commun.* **6**, 10177 (2015).
 - [27] S. Blankenburg, J. Cai, P. Ruffieux, R. Jaafar, D. Passerone, X. Feng, K. Müllen, R. Fasel, and C. A. Pignedoli, Intraribbon heterojunction formation in ultrananow graphene nanoribbons, *ACS Nano* **6**, 2020 (2012).
 - [28] P. Ordejón, E. Artacho, and J. M. Soler, Self-consistent order- n density-functional calculations for very large systems, *Phys. Rev. B* **53**, R10441 (1996).

- [29] J. M. Soler, E. Artacho, J. D. Gale, A. García, J. Junquera, P. Ordejón, and D. Sánchez-Portal, The siesta method for ab initio order- n materials simulation, *J. Phys.: Condens. Matter* **14**, 2745 (2002).
- [30] J. P. Perdew, K. Burke, and M. Ernzerhof, Generalized Gradient Approximation made Simple, *Phys. Rev. Lett.* **77**, 3865 (1996).
- [31] N. Troullier and J. L. Martins, Efficient pseudopotentials for plane-wave calculations, *Phys. Rev. B* **43**, 1993 (1991).
- [32] H. J. Monkhorst and J. D. Pack, Special points for Brillouin-zone integrations, *Phys. Rev. B* **13**, 5188 (1976).
- [33] K. Momma and F. Izumi, Vesta 3 for three-dimensional visualization of crystal, volumetric and morphology data, *J. Appl. Crystallogr.* **44**, 1272 (2011).
- [34] N. Papior, N. Lorente, T. Frederiksen, A. García, and M. Brandbyge, Improvements on non-equilibrium and transport green function techniques: The next-generation transiesta, *Comput. Phys. Commun.* **212**, 8 (2017).
- [35] M. Büttiker, Y. Imry, R. Landauer, and S. Pinhas, Generalized many-channel conductance formula with application to small rings, *Phys. Rev. B* **31**, 6207 (1985).
- [36] Z. Ma and W. Sheng, A spin-valve device based on dumbbell-shaped graphene nanoislands, *Appl. Phys. Lett.* **99**, 083101 (2011).
- [37] H. Sevinçli, M. Topsakal, E. Durgun, and S. Ciraci, Electronic and magnetic properties of 3d transition-metal atom adsorbed graphene and graphene nanoribbons, *Phys. Rev. B* **77**, 195434 (2008).
- [38] Y. Mao, J. Yuan, and J. Zhong, Density functional calculation of transition metal adatom adsorption on graphene, *J. Phys.: Condens. Matter* **20**, 115209 (2008).
- [39] C. Corona-García, G. H. Cocoletzi, and F. Sánchez-Ochoa, Adsorption of small pollutant molecules on monolayer blue phosphorus, *Mater. Today Commun.* **26**, 102123 (2021).
- [40] F. Sánchez-Ochoa, G. H. Cocoletzi, and G. Canto, Trapping and diffusion of organic dyes inside of palygorskite clay: The ancient Maya blue pigment, *Microporous Mesoporous Mater.* **249**, 111 (2017).
- [41] S. Boys and F. Bernardi, The calculation of small molecular interactions by the differences of separate total energies. Some procedures with reduced errors, *Mol. Phys.* **19**, 553 (1970).
- [42] M. Manadé, F. Viñes, and F. Illas, Transition metal adatoms on graphene: A systematic density functional study, *Carbon* **95**, 525 (2015).
- [43] V. Rigo, T. Martins, A. J. da Silva, A. Fazzio, and R. Miwa, Electronic, structural, and transport properties of Ni-doped graphene nanoribbons, *Phys. Rev. B* **79**, 075435 (2009).
- [44] Y.-E. Yang, Y. Xiao, X.-H. Yan, and C.-J. Dai, Transport properties of zigzag graphene nanoribbons adsorbed with single iron atom, *Chin. Phys. B* **24**, 117204 (2015).
- [45] C. Cocchi, D. Prezzi, A. Calzolari, and E. Molinari, Spin-transport selectivity upon co adsorption on antiferromagnetic graphene nanoribbons, *J. Chem. Phys.* **133**, 124703 (2010).
- [46] D. Wang, Z. Zhang, X. Deng, Z. Fan, and G. Tang, Magnetism and magnetic transport properties of the polycrystalline graphene nanoribbon heterojunctions, *Carbon* **98**, 204 (2016).
- [47] T. Chen, L. Wang, X. Li, K. Luo, L. Xu, Q. Li, X. Zhang, and M. Long, Spin-dependent transport properties of a chromium porphyrin-based molecular embedded between two graphene nanoribbon electrodes, *RSC Adv.* **4**, 60376 (2014).
- [48] S. Yuasa, T. Nagahama, and Y. Suzuki, Spin-polarized resonant tunneling in magnetic tunnel junctions, *Science* **297**, 234 (2002).
- [49] A. Voskoboinikov, S. S. Lin, C. Lee, and O. Tretyak, Spin-polarized electronic current in resonant tunneling heterostructures, *J. Appl. Phys.* **87**, 387 (2000).
- [50] D. J. Rizzo, G. Veber, J. Jiang, R. McCurdy, T. Cao, C. Bronner, T. Chen, S. G. Louie, F. R. Fischer, and M. F. Crommie, Inducing metallicity in graphene nanoribbons via zero-mode superlattices, *Science* **369**, 1597 (2020).
- [51] P. Ruffieux, S. Wang, B. Yang, C. Sánchez-Sánchez, J. Liu, T. Dienel, L. Talirz, P. Shinde, C. A. Pignedoli, D. Passerone, *et al.*, On-surface synthesis of graphene nanoribbons with zigzag edge topology, *Nature* **531**, 489 (2016).
- [52] W. Rojas, C. E. Villegas, and A. Rocha, Spin-orbit coupling prevents spin channel suppression of transition metal atoms on armchair graphene nanoribbons, *Phys. Chem. Chem. Phys.* **20**, 29826 (2018).
- [53] W. Y. Rojas, C. E. Villegas, and A. R. Rocha, Ab initio modelling of spin relaxation lengths in disordered graphene nanoribbons, *Phys. Chem. Chem. Phys.* **21**, 26027 (2019).
- [54] A. Cornia and P. Seneor, The molecular way, *Nat. Mater.* **16**, 505 (2017).